

Morphology, kinematics and modelling of the elliptical planetary nebula Sa 2-21

D. J. Harman,^{1*} M. Bryce,¹ M. P. Redman² and A. J. Holloway¹

¹*Jodrell Bank Observatory, Department of Physics & Astronomy, University of Manchester, Macclesfield, Cheshire SK11 9DL*

²*Department of Physics and Astronomy, University College London, Gower St., London WC1E 6BT*

Accepted 2003 February 24. Received 2003 February 13; in original form 2002 September 23

ABSTRACT

The little studied PN, Sa 2-21 has been observed using the Manchester echelle spectrometer at the Anglo-Australian telescope. Narrow band, long-slit spectra were obtained at six positions over two perpendicular position angles in both the [N II] $\lambda 6584$ Å and [O III] $\lambda 5007$ Å emission lines. An [O III] halo has been detected for the first time. A morphological modelling program was used to help determine the geometry, structure and kinematics of this ellipsoidal PN. It is proposed that the structure includes a pair of mid-latitude rings of [N II] emission, not previously seen in elliptical PNe. Radial spokes of [O III] emission have been detected in the main nebular shell indicating the presence of dynamical instabilities.

Key words: ISM: kinematics and dynamics – planetary nebulae: individual: Sa 2-21.

1 INTRODUCTION

Sa 2-21 (PN G238.9+07.3 = ESO 561-16) was discovered by Sanduleak (1975a,b) after being overlooked by the National Geographic-Palomar Sky Atlas possibly due to its close proximity (≈ 4 arcmin) to the photographic halo of the 4th magnitude star, 16 Puppis. Images are available at numerous wavelengths via SuperCOSMOS scans of UKST plates (Hambly et al. 2001a; Hambly, Irwin & MacGillivray 2001b; Hambly et al. 2001c); two of these are shown in Fig. 1. The general appearance of the planetary nebula (PN) is one of an ellipse, elongated along position angle $PA = 138^\circ$ (Corradi, Aznar & Mampaso 1998). No halo is seen in the H α and [O III] images of Schwarz, Corradi & Melnick (1992). Soker (1997) determines the morphology of Sa 2-21 as probably being the result of having had a substellar companion.

Acker et al. (1991) measured the H β flux as 11.9 ± 0.3 mW m $^{-2}$ while Cahn, Kaler & Stanghellini (1992) gives $T_e = 1.02 \times 10^4$ and He/H = 0.110. Preite-Martinez et al. (1991) calculated the energy-balance temperature of the central star as 72 000 K. Its inclusion in the NRAO VLA Sky Survey Condon & Kaplan (1998) gives its J2000 coordinates as RA 08^h08^m44^s.1 and Dec. $-19^\circ 14' 01''$ for the optical, and RA 08^h08^m44^s.30 \pm 0.3 and Dec. $-19^\circ 14' 05''.0 \pm 5''$ for the radio positions. The 1.4-GHz radio flux density was measured at $S_{1.4\text{ GHz}} = 5.4 \pm 1.0$ mJy with an H β extinction coefficient of $c = 0.1$. No coincident near infrared emission above background levels is seen in the *H*, *J* and *K* bands of the 2 Micron All-Sky Survey (2MASS – 2nd incremental release) images.

These observations were originally undertaken to provide data which could be compared to the computer simulations of the inter-

acting stellar winds models, for example (Frank & Mellema 1994, hereafter FM94). In particular the red images of this PN indicate a relatively uncomplicated tilted barrel structure, similar to the $\iota = 45^\circ$ model shown in fig. 2 of Frank et al. (1993) who compare the structure to the Owl nebula.

2 OBSERVATIONS

Sa 2-21 was observed with the Manchester echelle spectrometer (MES – Meaburn et al. 1984) situated at the *f*/8 focus of the Anglo-Australian Telescope (AAT) on the night of 1995 February 20. The 1024×1024 , 24- μ m square pixel TEK CCD was used with two-pixel binning in the spatial direction whilst leaving the wavelength axis at full resolution. Each unbinned pixel corresponds to 0.16 arcsec on the sky or a spectral resolution of 4.6 km s $^{-1}$. A filter of bandwidth 10 Å, centred on 6590 Å, was used to isolate the 87th echelle order containing the [N II] $\lambda 6584$ Å (henceforth [N II]) nebular emission line and a 25-Å bandwidth filter centred on 5010 Å was used for the 114th order [O III] $\lambda 5007$ Å (henceforth [O III]) line.

Sa 2-21 was observed at two perpendicular slit positions of $PA = 35^\circ$ and 125° , aligned along the equatorial and polar axes, respectively (based on measurements from images in Schwarz et al. 1992). Table 1 provides a summary of the exposures. A three-parallel-element slit mask was used at each PA, with a slit separation of 3.3 mm corresponding to 22.4 arcsec on the sky or 292 km s $^{-1}$ in velocity. Each individual slit is 70- μ m wide (≈ 0.47 arcsec on the sky and 6 km s $^{-1}$ in velocity) and is longer than the section imaged by the CCD. Two 1800-s exposures were taken at each position angle for each of the two emission lines. After each exposure and using exactly the same instrumental conditions, a Thorium Argon (ThAr) arc spectrum was taken for wavelength calibration. A short

*E-mail: dharman@jb.man.ac.uk

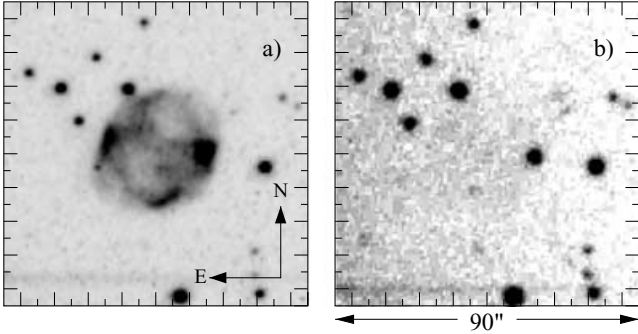


Figure 1. These images of Sa 2-21 are SuperCOSMOS scans of Schmidt survey plates. Each image is centred on the NRAO radio position and shows a $90 \times 90 \text{ arcsec}^2$ area of sky. The plates are (a) Short Red (4415 – OG590 – $\lambda 6500$), (b) Near Infrared (IVN – RG715 – $\lambda 7900$). The three values given in brackets after each title are the emulsion, filter and central wavelength (\AA) of the plate. The horizontal line towards the south of each frame is a diffraction spike from 16 Puppis.

Table 1. Observational summary of long-slit spectra from Sa 2-21 for the night of 1995 February 20. Listed are the position angle (PA), principle emission line, total exposure times, exposure start time and the average seeing conditions. The (+) sign indicates occasional, brief periods of seeing that was worse than that tabulated.

PA	Line	Exp. (s)	UT start	Av. Seeing
35°	[O III]	3600	09:59	2.3 arcsec
35°	[N II]	3600	11:16	2.5 arcsec
125°	[O III]	3600	12:37	3 arcsec+
125°	[N II]	3600	13:52	3 arcsec+

exposure of the PN and superimposed slit positions was taken at PA = 35° in [N II] and at PA = 125° in [O III]. The positions of the six slits are shown against the images in Fig. 2. Seeing varied from 2.3 to 3 arcsec and occasionally became poorer towards the end of the observing period due to patchy, light cloud.

3 RESULTS

3.1 General morphology

The structure of Sa 2-21 is quite different when seen in the [N II] and [O III] emission lines (see Fig. 2). A patchy structure is seen in the [N II] image where brighter ‘rings’ can be discerned. The ellipticity of the rings imply that the inclination (i) of the polar axis is closer to the plane of the sky rather than along the line of sight. The [O III] image is much smoother and almost symmetrical about the polar axis. The polar axis is aligned in a north-west to south-east orientation on the sky. The mild eccentricity and the projection of Sa 2-21 on the sky makes accurate measuring of the position angle of the polar axis imprecise. Through symmetry arguments the position angle of Sa 2-21 was determined to be at PA = 320°.

The coordinate system shown in Fig. 2 was found by fitting 21 star positions from the *United States Naval Observatory* (USNO) catalogue to the stars in the [N II] image of Sa 2-21. The position of the nebular centre was calculated from the symmetry of the PN as (J2000) RA 08^h08^m44^s.31 and Dec. $-19^\circ 14' 02''.3$, almost exactly coincident with the NRAO Sky Survey positions of Condon & Kaplan (1998). Note that the PN central star was not detected in these narrow band images.

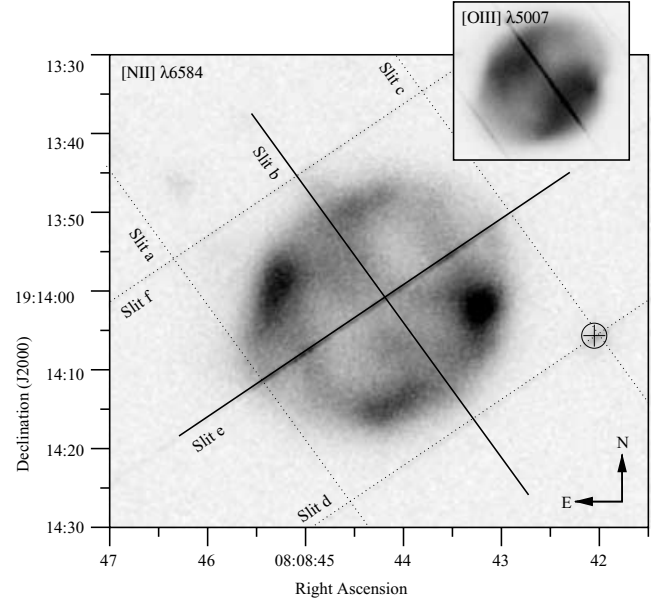


Figure 2. The main image is an [N II] exposure of Sa 2-21. Overlaid slit positions are shown at PA = 35° and 125°. The position-velocity (pv) arrays from slit positions b and e (solid lines) in [O III] and [N II] are shown in Figs 3 and 4, respectively. The cross marks the position of a star, see Section 3.2.2. The inset is an [O III] exposure shown at half scale to the main image with the PA = 35° slit positions superposed.

It is worth noting here the four areas of brighter emission seen in the red image of Fig. 1 and the narrow band [N II] image of Fig. 2, which occur at each ‘corner’ of Sa 2-21. The reason why the western blob is apparently so much brighter than the others becomes clear when the optical images are compared to the near-infrared Schmidt plate scan, which shows the position of a star directly behind this blob.

3.2 Long-slit observations

Although a three-element multislit was used, only the central slit at each position angle passes through the PN. The outer two slits at PA = 35° just graze the polar extremities.

The heliocentric radial velocity (V_{hel}) of Sa 2-21 was determined from the centre of ellipses fitted to the position-velocity profiles. A mean value of $V_{\text{hel}} = 102 \text{ km s}^{-1}$ was measured from the two central slits (b and e) in both emission lines. As both of these slits pass very close to the nebular centre, this is likely to be very close to its true value.

3.2.1 Slit e – PA=125°

Slit e bisects Sa 2-21 almost directly through the centre of the PN. It is rotated at a position angle of about 5° away from that of the polar axis. As can be seen by the position-velocity (pv) arrays in Fig. 3, the profiles in [O III] and [N II] are quite different from each other, although they follow the same basic underlying shape. The [O III] emission can be seen to lie primarily in a bright waistband. There is a sharp border between this strong emission napkin ring and the weaker emission poles.

The striking features of the [N II] emission pv array are the bright blobs which appear on a faint ellipse. Two pairs of these blobs appear

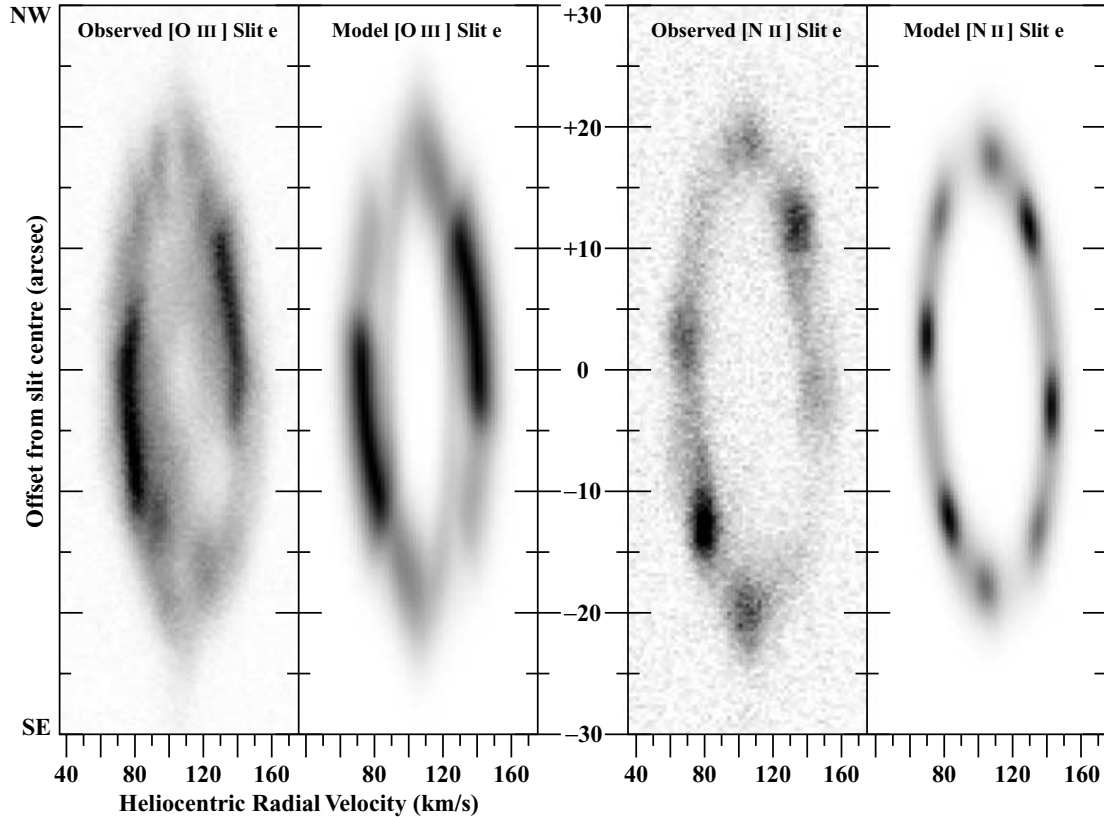


Figure 3. Position velocity arrays of Sa 2-21 in the [O III] and [N II] emission lines from slit e are shown in the left hand side of each of the two panels. Corresponding model data is displayed in the right hand side of each panel. The horizontal axis is corrected to heliocentric radial velocity (V_{hel}). The vertical axis is 60 arcsec long and corresponds spatially to the solid line (slit e) in Fig. 2.

coincident with the top and bottom of the waistband seen in the [O III] pv array. This implies that the [N II] emission is concentrated into two narrow mid-latitude rings, parallel to the equatorial plane tracing the change in emission in the broad [O III] waistband. This in turn would mean that the four areas of brighter emission seen in the [N II] image (Fig. 2, Section 3.1) are the limb-brightened edges of these rings rather than individual knots of emission. Two further blobs are obvious in the [N II] pv array, one each at the top and at the bottom of the profile. Their symmetry in the velocity ellipse implies that they originate from the same latitude above and below the equatorial axis. These will be covered in greater depth in Section 4.

The two high-latitude [N II] knots appear to coincide with gaps in the [O III] emission towards the poles. The faint spatially extended [O III] emission to the top and bottom of the profile indicate the presence of a faint [O III] halo. Note that slits d and f (not shown here) which are situated beyond the main shell also show faint [O III] emission, supporting the idea that this PN has a faint [O III] halo. No corresponding [N II] halo is seen. Determining the [O III] emission morphology of Sa 2-21 in its polar regions is complicated due to the contamination of this faint halo.

3.2.2 Slit b – $PA=35^\circ$

The pv arrays generated by slit b (Fig. 4) form an unbroken ellipse in both emission lines. The slit position cuts Sa 2-21 across the equatorial axis, slightly offset from the centre towards the north-

west pole. This causes it to graze the nearside edge of the bright [O III] napkin ring and [N II] mid-latitude ring structures. This generates features in the pv arrays of both emission lines. The effect of grazing the edge of the waistband in [O III] shows up as a deviation from an almost perfect ellipse in the pv array. This deviation shows as lower systemic expansion velocities in the blueshifted north-east quarter of the profile. This (upper-left) quadrant of the [N II] ellipse profile is obviously different from the rest of the pv array. The high emission is caused by grazing a mid-latitude ring whereas the remainder is produced by the lower emission equatorial regions. An ‘indent’ in the profile occurs centred on an offset of -4 arcsec in the blueshifted half of the [N II] ellipse.

The [N II] pv array shows up a very interesting feature in that the inner boundary, both in spatial position and velocity spread, is very well defined. This very sharp inner boundary to the [N II] ionization zone is quite unlike the [O III] ionization zone which extends a significant distance into the centre of the PN (as seen from $V_{\text{sys}} = 0 \text{ km s}^{-1}$; $V_{\text{hel}} = 102 \text{ km s}^{-1}$) and out from the obvious strongly emitting shell.

Radial streams can be seen in the [O III] pv array, originating from the main ellipse. These intriguing features are most apparent at the top and bottom ends of the ellipse. Slightly different grey-scale presentations reveal more of these features further down and up the array. It should be noted that the halo appears stronger at the north-west side of the pv profile ($+20$ arcsec offset). This, however, is partially due to the continuum spectrum of a star produced by slit c, whose position is marked in Fig. 2.

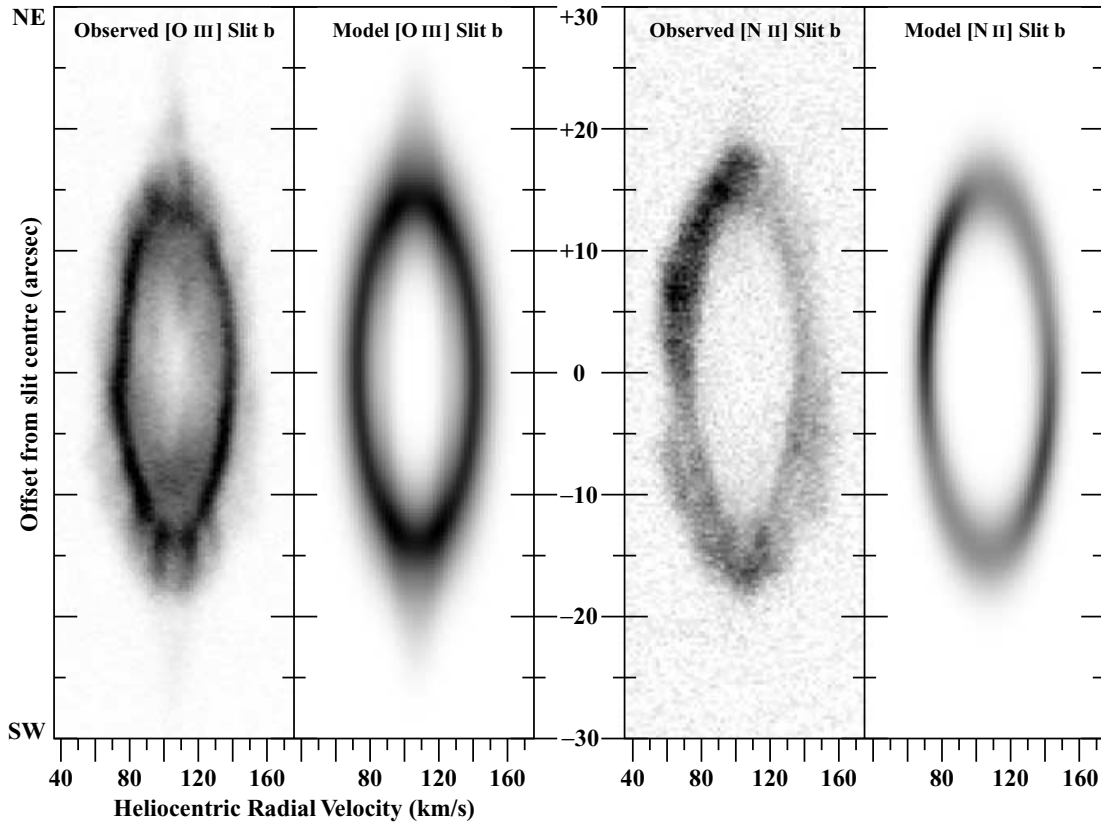


Figure 4. Position velocity arrays of Sa 2-21 in the [O III] and [N II] emission lines from slit b are shown in the left-hand side of each of the two panels. Corresponding model data is displayed in the right-hand side of each panel. The horizontal axis is corrected to heliocentric radial velocity (V_{hel}). The vertical axis is 60 arcsec long and corresponds spatially to the solid line (slit b) in Fig. 2.

4 DISCUSSION

4.1 Compact radial velocity spokes

The radial features seen at the south-west end of the [O III] profile in Fig. 4 (see Section 3.2.2), in particular, appear to curve towards a constant velocity.

These faint radial spokes have been visually enhanced by deconvolution with a two-dimensional Moffat function, with axes defined by the seeing conditions in the spatial dimension and the velocity resolution in the velocity dimension. The results are shown in Fig. 5, where several faint radial spokes can now be seen surrounding the emission ellipse. (Trujillo et al. 2001 show that a Moffat function is closer to observed stellar profiles than a Gaussian.) Similar shaped PNe to Sa 2-21 have been modelled by FM94 using a hydrodynamical simulation. Mellema (1994, 1995) also show models which are morphologically similar to Sa 2-21 and show a dense equatorial waist structure with decreasing emission toward the lower density poles. Sa 2-21 lies somewhere between FM94's models A and B. In these models a similar, bright equatorial [O III] band develops, with emission decreasing with increasing latitude. Note the similarities between the $\iota = 25^\circ$ projections (FM94 fig. 4) and our observations. The long-slit spectra (FM94 fig. 5) are more difficult to compare due to the high resolution (absence of observational broadening effects) of their synthetic pv arrays. A further similarity between FM94's models and our observations is the velocity vector plot for model A (reproduced in Fig. 5). Note the regular radial features in Fig. 5 and compare to those on the observed [O III] pv array of Fig. 4. Of course, the velocity vector plot and the pv

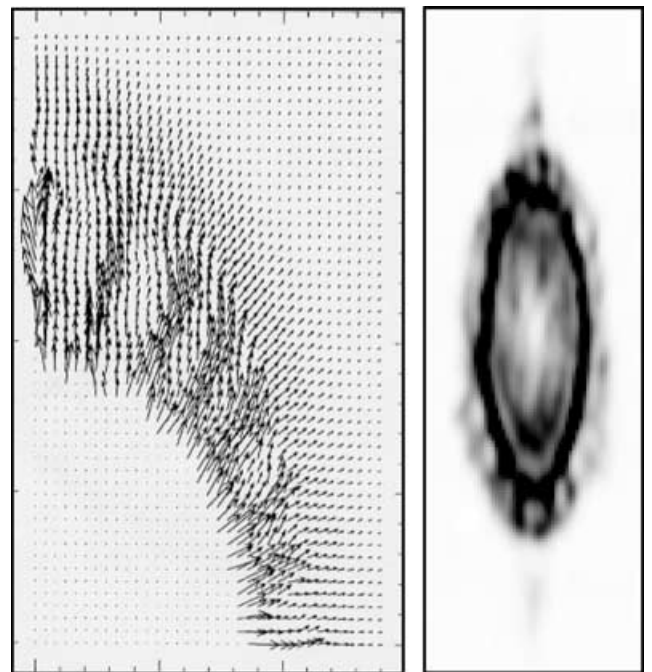


Figure 5. Left-hand panel: velocity vector plot for model A after $t = 783$ yr. See fig. 2 of Frank & Mellema (1994) for full explanation. Reproduced by permission of the AAS. Right-hand panel: [O III] slit b pv array after deconvolution to highlight spokes (cf. Fig. 4).

array are not the same type of plot, but if the emission follows the model kinematics then something similar to the observed velocity profile could be produced. FM94 comment that the radial features are primarily a numerical effect but that the inner shock may be subject to a corrugation instability.

If the pressure interior to the shell builds up then the shell can become prone to instabilities. For example, a dense shell that is accelerating (due to either a rapid drop in the external density or to an increased pressure from within the shell) may break up via the Rayleigh–Taylor instability. Alternatively, in thin shells, dynamical overinstabilities can also lead to a shell breaking up into fragments (Mac Low & Norman 1993). In both cases, the fragments produced will have sizes of the order of the shell thickness. Once the shells have begun to fragment, then the hot interior gas is free to escape through the gaps that begin to form. Eventually, the shell gas is confined to clumps with the interior gas flowing past causing shocks to drive into the clumps and ablation of material from them into the flow.

The early stages of such a process may be taking place within Sa 2-21. The higher ionization [O III] emitting gas is confined, for the most part, closer to the central star than the [N II] emitting gas. However, thin velocity spokes of [O III] are clearly discerned (see Fig. 4) that are coincident and even lying beyond the [N II] emitting gas. The [O III] emitting gas may therefore be escaping at discrete points into the [N II] region. These spokes are most prominent at the projected edges of the nebula becoming much fainter toward the centre of the nebula. This is because the spokes are spatially dispersed but their velocity range is small and so towards the centre of the nebula they tend to blend with the emission from the velocity ellipse. The separation of the individual spokes is explicable as the fastest-growing modes of the RT instability are those of the order of the shell thickness; the [O III] gas escapes through weak points separated by approximately this distance.

4.2 Mid-latitude rings

The distribution of the [N II] emission could be explained by the presence of two mid-latitude rings, as modelled here. Such a feature would be unique amongst planetary nebulae if the emission were confined to two rings but in fact fainter [N II] emission is visible at lower latitudes, coincident with the [O III] emission. The pv arrays indicate that the [O III] emission is quite ‘filled in’ compared to the [N II] and therefore occupies the inner volume of the nebula with the [N II] lying beyond it. The enhanced brightness of the [N II] that causes the rings is not straightforward to explain. If the mechanism for forming the velocity spokes described above is operative then perhaps the brightest regions are those portions of the earlier shell that have not yet been disrupted by the mixing of the [O III] and [N II] emitting gas. In other words, the previous shell (with gaps at the poles) has been disrupted at equatorial latitudes and this disruption is proceeding towards the poles. This would require an equatorial outflow or ejection from the central star.

An alternative explanation could be that the [N II] emission arises at the edge of a biconical outflow that has recently propagated within the approximately spherical nebula. If the main body of the nebula has a shell structure then a biconical outflow could generate a ring morphology as it breaks through the shell. An example of such an outflow (though with an outflow axis close to the plane of the sky) may be CRL 2688, the Egg nebula, which is a protoplanetary nebula that could be at the transitional stage between a mostly spherical AGB mass-loss phase and a bipolar planetary nebula. In CRL 2688, the ‘searchlight beams’ have an opening angle of $\sim 15^\circ$ (Sahai et al.

1998), whereas in our model of Sa 2-21 the opening angle is much wider.

The impact of the outflow on the pre-existing shell would then be cause of the break-up and mixing of the two ionized gas components. Perhaps it is also worth pointing out that Sa 2-21 has morphological similarities to the Dumbell nebula and that this nebula also has spots of enhanced low-ionization material (in this case, neutral hydrogen) that lie at the edges of the central higher ionization regions.

Hydrodynamic models may also be able to explain the rings through a global nebula instability. Two-dimensional models such as those of Borkowski, Blondin & Harrington (1997) show instabilities in a PN shell caused by hydrodynamic collimation of a bipolar outflow. Similarly, García-Segura et al. (1999) develop 2D magnetohydrodynamic models of PN in which shell instabilities are seen. The latter authors use their 2D results to simulate the 3D appearance of the nebula (by rotating around the symmetry axis). The instabilities then appear as rings in the plots. Of course, it is not at all clear whether fully 3D models would produce such ring features. It seems more likely that the instabilities would be more localized, though if they formed preferentially at a particular ‘latitude’ then the overall emission could be that of a ring.

4.3 High-latitude rings

The two bright blobs at the top and bottom of the PA = 125 [N II] pv profile (Fig. 3) require more discussion. These might naively be assumed to originate as emission from polar caps. However, because the polar axis of the nebula is inclined to the plane of the sky, then, assuming that the nebula expands radially from the central star, any such polar cap would have a velocity component along the line-of-sight and hence would appear at a position offset from the end of this observed pv ellipse in an anti-clockwise direction.

Here we propose that these two blobs arise from two high-latitude rings of emission. The obvious problem with this hypothesis is that each blob should have a partner arising from the other side of the ring (compare with the pairs of blobs arising from each mid-latitude ring). The nearside (blueshifted) portion of the north-west ring and the opposite far-side (redshifted) portion of the south-east ring are not obvious in the pv profile. The missing blobs should appear on the [N II] ellipse at around ± 17 arcsec.

5 MODEL

A 3D morphological modelling program was developed to model basic PN and nova shell morphologies and kinematics and produce synthetic images and pv arrays at slit positions across the model (Harman 2001).

A cubic grid with sides of length 60 arcsec and with resolution of 0.32 arcsec pix^{-1} was used for the computations. Synthetic pv arrays were produced with the same velocity range and both velocity and spatial resolution as in the observed data.

This meant that real and model data could be directly compared, hence differences could be discerned and the model fine tuned. An iterative routine of comparing and adjusting the models parameters brought it into close agreement with the observations.

Convolution was used to take into account the seeing conditions (see Table 1) when generating the model images (shown in Fig. 6) and calculating what emission is added to and removed from the slits view when generating synthetic pv spectra. Likewise, the instrumental velocity resolution of 6 km s^{-1} is reproduced in a similar way for the pv spectra.

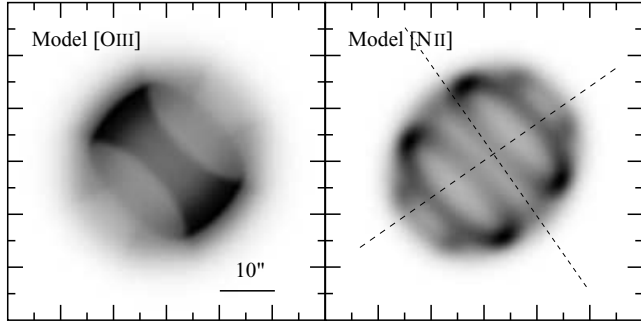


Figure 6. 2D image projections of the model that produced the synthetic pv arrays (shown in Figs 3 and 4), for comparison with the observed images of Sa 2-21 shown in Fig. 2. The positions of the synthetic slits through which the model pv arrays were generated are marked, as is the scale. Note that the model images have been convolved to match the seeing at time of observation.

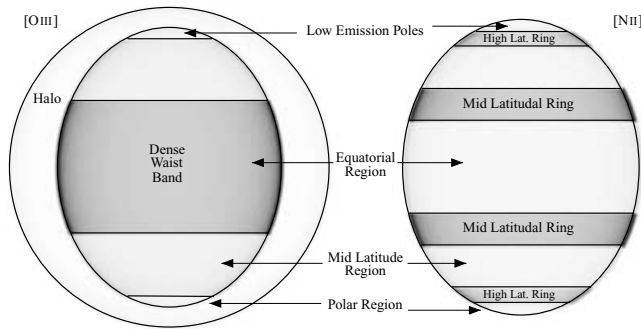


Figure 7. Projections of the (left-hand panel) [O III] and (right-hand panel) [N II] models. Outlines are included to aid the eye in delineating the changes in emission. Important features on each emission model are labelled.

The expansion velocity, v , of any point in the 3D grid is a linear function of radial distance, r , from the centre of the model; $v = kr$, where k is the expansion constant (in $\text{km s}^{-1} \text{arcsec}^{-1}$) defined for each shape within the model.

5.1 Model parameter summary

An ellipsoid is used for the main shell at a 1.25:1 polar to equatorial axis ratio orientated at $\text{PA} = 315^\circ$ and $i = 70.2^\circ$. The [O III] and [N II] morphologies are quite different and hence two separate models were used. Fig. 7 and Table 2 provide a graphical and textual summary of the morphologies of the two models. In real PNe,

Table 2. Summary of angular emission changes in the [N II] and [O III] models of Sa 2-21.

Emission model	Latitudinal range	comment
[O III]	0° – 34°	Dense waistband
[O III]	34° – 70°	Mid latitude region
[O III]	70° – 90°	Polar region
[O III]	0° – 90°	Halo
[N II]	0° – 22°	Equatorial region
[N II]	22° – 38°	Mid latitude rings
[N II]	38° – 60°	Mid latitude region
[N II]	60° – 70°	High latitude rings
[N II]	70° – 90°	Polar region

ionization stratification results in the [O III] emitting region being produced closer to the central star than the [N II] region. This results in difference in spatial size which is seen clearly in the two observed pv spectra and hence is used in the two models.

5.1.1 [O III] model

The [O III] model was composed of an ellipsoid of semi-major/minor axis lengths of 17.5 and 14 arcsec. The expansion for the shell was calculated from an expansion constant of $k = 2.4 \text{ km s}^{-1} \text{arcsec}^{-1}$, hence the poles and equator were expanding at 42 and 33.6 km s^{-1} , respectively.

The emission morphology of the ellipse is constructed by a number of emission changes which happen at specified degrees of latitude from the equator (0°) to the poles (90°) as measured from the centre of the model. The high-density waistband of the main shell exists between latitudes of $\pm 34^\circ$. A drop in emission occurs here, continuing up to an angle of 69° where it drops again. This very low emission continues up to the poles.

The [O III] model includes an additional sphere for the faint halo which has a radius of $20''$, and an expansion velocity of 16.8 km s^{-1} , ($k = 0.8 \text{ km s}^{-1} \text{arcsec}^{-1}$). The model halo is isotropic.

5.1.2 [N II] model

The [N II] model has a semi-major/minor axis length of 18.5 and 14.8 arcsec, respectively. Using the same expansion constant as in [O III], $V_{\text{exp}} = 44.4$ and 35.5 km s^{-1} result for the poles and equator, respectively.

The emission morphology of the [N II] model is slightly more complicated than the [O III] model. The mid-latitude rings occur between 22° and 38° from the equator, the high latitude rings between 60° and 70° . The polar regions are lower in emission than the equatorial and mid-latitude regions which are, in turn, much lower than the high emission rings.

The outer limbs of the mid-latitude rings appear brighter in Fig. 7 than the limbs closer to the nebular centre. This is a limb brightening effect resulting from the fact that the ellipsoidal shell is thin compared to the latitudinal extent of the ring.

6 CONCLUSION

We have presented high-resolution, long-slit spectral data of Sa 2-21 and have determined its three-dimensional structure in the [N II] and [O III] emission lines. A halo around this PN is reported for the first time. The halo is observed in [O III] emission but not detected in [N II]. The tilted barrel shape indicated by the images of this PN is found to be consistent with the spectral data, however these data also indicate several more complex features which are not predicted by the interacting stellar winds model. Pairs of bright knots in the [N II] spectra indicate the presence of two mid-latitude rings. Such rings are known to exist, and have been found to be a fairly common phenomenon, in bipolar PNe such as MyCn 18 (Sahai et al. 1999), and He 2-104 (Corradi et al. 2001). However, the discovery of mid-latitude rings in an elliptical PN is, to the best of our knowledge, unique. Bright knots at either end of the [N II] velocity ellipse are interpreted as possibly arising from a further set of high latitude rings.

A regular pattern of radial flows has been observed in the bright equatorial [O III] band. These are thought to be due to RT instabilities causing break-up of the shell and mixing to occur through the holes produced.

A morphological modelling program was used to investigate the 3D structure. An axially symmetric model, with velocity given by a linear function of radial distance from the centre of the nebula was adopted. The inclusion of mid-latitude and high-latitude rings produced results in excellent agreement with our observations.

ACKNOWLEDGMENTS

We wish to thank the staff at the AAT for their excellent assistance during the observations in 1995 February. The source positions were provided by observations from the joint NASA/USNO/NRAO geodetic/astrometric observing program and the positions are in the frame of the ICRF-Ext.1 catalog. We have made use of the UKST archive, Royal Observatory, Edinburgh, and the NASA/ IPAC Infrared Science Archive, which is operated by the Jet Propulsion Laboratory, California Institute of Technology, under contract with the National Aeronautics and Space Administration. DJH wishes to thank Wolfgang Steffan for making the SHAPE code available in its original form for further development and upgrading. DJH acknowledges a PPARC studentship and subsequent Research Associateship at Jodrell Bank. MPR is supported by PPARC. Finally we wish to thank the anonymous referee for his/her swift and helpful comments.

REFERENCES

- Acker A., Raytchev B., Stenholm B., Tylanda R., 1991, *A&AS*, 90, 89
 Borkowski K. J., Blondin J. M., Harrington J. P., 1997, *ApJ*, 482, L97
 Cahn J. H., Kaler J. B., Stanghellini L., 1992, *A&AS*, 94, 399
 Condon J. J., Kaplan D. L., 1998, *ApJS*, 117, 361
 Corradi R. L. M., Aznar R., Mampaso A., 1998, *MNRAS*, 297, 617
 Corradi R. L. M., Livio M., Balick B., Munari U., Schwarz H. E., 2001, *ApJ*, 553, 211
 Frank A., Mellema G., 1994, *ApJ*, 430, 800
 Frank A., Balick B., Icke V., Mellema G., 1993, *ApJ*, 404, L25
 García-Segura G., Langer N., Różyczka M., Franco J., 1999, *ApJ*, 517, 767
 Hambly N. C. et al., 2001a, *MNRAS*, 326, 1279
 Hambly N. C., Irwin M. J., MacGillivray H. T., 2001b, *MNRAS*, 326, 1295
 Hambly N. C., Davenhall A. C., Irwin M. J., MacGillivray H. T., 2001c, *MNRAS*, 326, 1315
 Harman D. J., 2001, PhD thesis, Univ. Manchester
 Mac Low M., Norman M. L., 1993, *ApJ*, 407, 207
 Meaburn J., Blundell B., Carling R., Gregory D. F., Keir D., Wynne C. G., 1984, *MNRAS*, 210, 463
 Mellema G., 1994, *A&A*, 290, 915
 Mellema G., 1995, *MNRAS*, 277, 173
 Preite-Martinez A., Acker A., Koeppen J., Stenholm B., 1991, *A&AS*, 88, 121
 Sahai R. et al., 1998, *ApJ*, 493, 301
 Sahai R. et al., 1999, *AJ*, 118, 468
 Sanduleak N., 1975a, *Pub. of the Warner and Swasey Obs.*, 2, No. 1
 Sanduleak N., 1975b, *PASP*, 87, 705
 Schwarz H. E., Corradi R. L. M., Melnick J., 1992, *A&AS*, 96, 23
 Soker N., 1997, *ApJS*, 112, 487
 Trujillo I., Aguerri J. A. L., Cepa J., Gutiérrez C. M., 2001, *MNRAS*, 328, 977

This paper has been typeset from a \LaTeX file prepared by the author.